JOURNAL OF PROPULSION AND POWER
Vol. 24, No. 5, September–October 2008

Numerical Simulation of Direct Current Glow Discharges for High-Speed Flow Control

Jonathan Poggie*
U.S. Air Force Research Laboratory, Wright–Patterson Air Force Base, Ohio 45433-7512

DOI: 10.2514/1.24403

Numerical studies of glow discharges were carried out to evaluate their utility for flow control applications. As part of this project, a three-dimensional computer code has been written to solve the fluid conservation laws, the charged particle continuity equations under the drift-diffusion model, and the Poisson equation for the electric potential. Glow discharge calculations have been carried out in the absence of flow, exploring the effects of background pressure, applied magnetic fields, and finite electrodes. With the presence of a Mach 5 crossflow, three-dimensional computations have identified the origin of the downward force in a "plasma flap" concept as dissipative heating in the vicinity of the cathode, and rough agreement has been obtained between numerical predictions and experimental measurements of the total temperature rise in that region. A simplified actuator model has been applied in the numerical exploration of the control of a Mach 14 compression ramp flow, and suitable actuator locations and power levels have been identified.

I. Introduction

INTEREST in electromagnetic control of high-speed flows dates to the mid-1950s, when the problem of hypersonic atmospheric entry was first being explored. Given the high temperatures in the shock layer around a reentry vehicle, and the concomitant ionization and electrical conductivity, it was natural to consider exploiting electromagnetic effects for flow control. Interest in large-scale aerospace magnetohydrodynamics has waxed and waned several times in the intervening decades, with the initial enthusiasm eventually dampened each time by the realities of the weight and complexity of high-strength magnets and power conditioning equipment.

Because of the nonlinear scaling of the weight of this equipment with actuator size, small-scale actuators are not prohibitively heavy. For example, a magnet capable of generating a field of order 1 T over a meter extent weighs on the order of tons (e.g., a medical magnetic resonance imaging machine), whereas the same field strength applied over a centimeter can be obtained with a permanent magnet that can be held (with care) in the hand. Thus, small-scale plasma actuators are currently considered to be a promising means of flow control for application in both propulsion and external aerodynamics.

This paper reviews numerical studies carried out by the author on the use of dc glow discharges for local flow control. Because nonneutrality near electrode surfaces is an essential feature of glow discharge behavior, a prototype computer code is being developed to model space charge effects.

In the initial work, this code was applied to two-dimensional simulations of glow discharges in the normal glow regime in the absence of bulk gas flow [1,2]. Two-dimensional discharges were also explored with finite electrodes in the abnormal glow regime [3]. This work was later extended to three dimensions, with the effects of varying background pressure and the applied magnetic field examined [4,5].

The control of a two-dimensional, low Reynolds number airfoil flow was explored [2,4] but was found to be relatively ineffective. Greater success was obtained with calculations for a Mach 5 flat plate boundary-layer flow [2,4,5], which compared reasonably with the experimental data of Menart et al. [6].

Recent work has avoided the computational cost of high-fidelity discharge modeling by employing a simplified model of the mechanical and thermal energy inputs introduced by a plasma actuator. In particular, a Mach 14 compression ramp flow has been studied, and locations have been identified in which a modest power input can result in significant structural changes to the flow [7].

This paper presents selected results from this work. First, the physical model and numerical methods are outlined (Sec. II). Then, a simple, three-dimensional calculation of a discharge in the normal glow regime is described (Sec. III). The discharge model is next applied to the Mach 5 boundary-layer flow, which represents a simple "plasma flap" concept (Sec. IV). Finally, the simplified model is applied to the Mach 14 compression ramp flow (Sec. V).

This work aims to demonstrate that, for a reasonably simplified physical model, three-dimensional computations of glow discharge actuators are feasible. Additional research on more efficient algorithms is necessary to enable routine engineering calculations of actuator performance.

II. Methods

A three-dimensional computer code has been written to solve the bulk-flow conservation laws, drift-diffusion equations, and Poisson equation in an implicit, loosely coupled fashion. Several numerical techniques, including proper evaluation of the source terms and implicit procedures, have proven to be critical to successful high-fidelity simulations.

A. Physical Model

The conservation of mass, momentum, and energy for the overall gas is expressed as

$$\frac{\partial \rho}{\partial t} + \nabla \cdot (\rho \mathbf{u}) = 0 \tag{1}$$

$$\frac{\partial}{\partial t}(\rho \mathbf{u}) + \nabla \cdot (\rho \mathbf{u}\mathbf{u} - \boldsymbol{\Sigma}) = \mathbf{f} \tag{2}$$

$$\frac{\partial \mathcal{E}}{\partial t} + \nabla \cdot (\mathbf{u}\mathcal{E} - \boldsymbol{\Sigma} \cdot \mathbf{u} + \mathbf{Q}) = \mathbf{f} \cdot \mathbf{u} + S \tag{3}$$

Received 3 April 2006; revision received 14 March 2008; accepted for publication 14 March 2008.

*Senior Aerospace Engineer, Computational Sciences Center. Associate Fellow AIAA.

where ρ is the gas density, $\mathbf{u}$ is its velocity, $\mathbf{\Sigma}$ is the total stress tensor, $\mathcal{E} = \rho(\epsilon + u^2/2)$ is the total fluid energy, ϵ is the internal energy, and $\mathbf{Q}$ is the heat flux. The total stress tensor $\mathbf{\Sigma}$ is given by the usual constitutive equation for a Newtonian fluid, and the heat flux $\mathbf{Q}$ follows Fourier's heat conduction law. The source terms on the right-hand sides of the conservation equations include a body force $\mathbf{f}$ and a dissipative energy source S. Simplified models of these source terms will be discussed in Sec. V.

In the detailed plasma model, the body force is $\mathbf{f} = \rho_c \mathbf{E} + \mathbf{j} \times \mathbf{B}$ and the total energy delivered to the fluid by electromagnetic effects is $\mathbf{f} \cdot \mathbf{u} + S = \mathbf{E} \cdot \mathbf{j}$. The mass density, the charge density, and the total current density are found by summing over all the species: $\rho = \Sigma_s m_s n_s$, $\rho_c = \Sigma_s q_s n_s$, and $\mathbf{j} = \Sigma_s q_s n_s \mathbf{v}_s$, where m is the mass per particle, n is the species number density, q is the charge per particle, and $\mathbf{v}$ is the species velocity.

At present, a vibrational energy equation is not incorporated into the model. Following the simplified treatment of vibrational nonequilibrium commonly used in the literature [8], the energy deposition term $\mathbf{E} \cdot \mathbf{j}$ in Eq. (3) is replaced with $\eta \mathbf{E} \cdot \mathbf{j}$, where $1 - \eta$ represents the fraction of energy delivered to vibrational modes. Here we take $\eta = 0.1$.

Neglecting acceleration terms and diffusion due to temperature gradients, the particle and momentum conservation equations for each species can be combined to obtain a drift-diffusion model:

$$\frac{\partial n_s}{\partial t} + \nabla \cdot \{n_s[\mathbf{u} + s_s \mu_s \mathbf{M}^s \cdot (\mathbf{E} + \mathbf{u} \times \mathbf{B})]\} = \nabla \cdot (D_s \mathbf{M}^s \cdot \nabla n_s) + \omega_s \tag{4}$$

where s_s is the sign of q_s, and the tensor $\mathbf{M}^s$ is defined as

$$M^s_{ij} = \frac{1}{1 + \mu_s^2 B^2} \left(\delta_{ij} + \mu_s^2 B_i B_j + s_s \mu_s \epsilon_{ijk} B_k \right) \tag{5}$$

The dot product in Eq. (4) corresponds to summation on the second index of M_{ij}.

For the present work, two species of charged particles are considered (ions and electrons, denoted here by the subscripts i and e), and the charged particle generation rate is taken to have the form

$$\omega_{i,e} = \alpha \Gamma_e - \beta n_i n_e \tag{6}$$

where α is the ionization coefficient, β is the recombination coefficient, and Γ_e is the magnitude of the electron flux relative to the bulk gas flow. All the discharge calculations presented in this paper were carried out for nitrogen gas. Data for the mobilities, diffusion coefficients, ionization coefficient, and recombination coefficient were taken from [9].

The electric potential is determined from the Poisson equation

$$\nabla^2 \phi = -\rho_c / \epsilon_0 \tag{7}$$

where ϵ_0 is the permittivity of free space, and the electric field is found from $\mathbf{E} = -\nabla \phi$.

Conventional no-slip wall conditions and inlet/outlet boundary conditions were used for the fluid equations. The normal component of the ion flux was assumed to be zero at the anode, and the normal component of the electron flux at the cathode was found from the relation

$$\Gamma_e \cdot \mathbf{n} = -\gamma \Gamma_i \cdot \mathbf{n} \tag{8}$$

where γ is the secondary emission coefficient, $\mathbf{n}$ is a unit normal vector, and the species fluxes $\Gamma_{i,e}$ were computed using one-sided, second-order spatial differences. The potential at the anode was taken to be zero. The cathode potential V_c was either held fixed or determined according to an external circuit such that $V_c = -V + IR$, where V is the applied voltage, R is the external resistance, and I is the total current at the anode.

B. Numerical Methods

The conservation laws were solved using approximately factored, implicit schemes related to those developed by Beam and Warming [10], Pulliam [11], and Surzhikov and Shang [9]. Applying the standard transformation from physical coordinates (x, y, z) to grid coordinates (ξ, η, ζ), the conservation equations (1–4) can be written in the form

$$\frac{\partial \bar{U}}{\partial t} + \frac{\partial \bar{E}}{\partial \xi} + \frac{\partial \bar{F}}{\partial \eta} + \frac{\partial \bar{G}}{\partial \zeta} = \frac{\partial \bar{E}_v}{\partial \xi} + \frac{\partial \bar{F}_v}{\partial \eta} + \frac{\partial \bar{G}_v}{\partial \zeta} + \bar{S} \tag{9}$$

where, for example, $\bar{U} = U/J$, $\bar{E} = (\xi_x E + \xi_y F + \xi_z G)/J$, and for the fluid conservation laws $U = [\rho, \rho u_x, \rho u_y, \rho u_z, \mathcal{E}]^T$. (Here, J is the Jacobian of the grid transformation).

Writing Eq. (9) as $\partial \bar{U}/\partial t = R$, and discretizing in time, we have

$$(1 + \theta)\bar{U}^{n+1} - (1 + 2\theta)\bar{U}^n + \theta \bar{U}^{n-1} = \Delta t R^{n+1} \tag{10}$$

where $\theta = 0$ for an implicit Euler scheme and $\theta = 1/2$ for a three-point backward scheme. We introduce subiterations such that $\bar{U}^{n+1} \to \bar{U}^{p+1}$, with $\Delta \bar{U} = \bar{U}^{p+1} - \bar{U}^p$. The right-hand side R^{n+1} is linearized in the standard "thin-layer" manner. Collecting the implicit terms on the left-hand side and introducing approximate factoring and a subiteration time step $\Delta \hat{t}$ gives an equation set of the form

$$\mathcal{L}_\xi \mathcal{L}_\eta \mathcal{L}_\zeta \Delta \bar{U} = -\frac{\Delta \hat{t}}{1 + \theta} \left\{ \frac{(1 + \theta)\bar{U}^p - (1 + 2\theta)\bar{U}^n + \theta \bar{U}^{n-1}}{\Delta t} - R^p - D_e \bar{U}^p \right\} \tag{11}$$

where $\mathcal{L}_\xi$, $\mathcal{L}_\eta$, and $\mathcal{L}_\zeta$ are implicit spatial difference operators.

For the bulk fluid conservation laws, the scheme employs the implicit and explicit damping operators described by Pulliam [11]. The explicit damping operator D_e uses a nonlinear blend of second- and fourth-order damping [12]. The spatial derivatives are evaluated using second-order central differences.

For the drift-diffusion equations, no damping is used. Instead, these equations are discretized in space using a second-order upwind scheme based on the convection-drift velocity $\mathbf{V}_s = \mathbf{u} + s_s \mu_s \mathbf{M}^s \cdot (\mathbf{E} + \mathbf{u} \times \mathbf{B})$. A second-order, upwind method was also applied when calculating the species fluxes present in the source terms. (See the discussion of the charged particle generation term in [5,9].)

The Poisson equation is solved using an approximately factored implicit scheme adapted from the approach described by Holst [13,14]. Applying the usual transformation of coordinates, the three-dimensional Poisson equation (7) can be written in the form

$$\frac{\partial \phi}{\partial \tau} = \frac{\partial \bar{E}}{\partial \xi} + \frac{\partial \bar{F}}{\partial \eta} + \frac{\partial \bar{G}}{\partial \zeta} - \bar{S} \tag{12}$$

where the left-hand side is an artificial time term that motivates an iterative procedure for driving the right-hand side toward zero. We write $\Delta \phi / \Delta \tau = L\phi^{p+1}$, where $\Delta \phi = \phi^{p+1} - \phi^p$. We then linearize the right-hand side using the standard thin-layer approach, introduce $\alpha = 1/\Delta \tau$, an overrelaxation parameter ω, and approximate factoring. This gives

$$\mathcal{L}_\xi \mathcal{L}_\eta \mathcal{L}_\zeta \Delta \phi = \omega \alpha^{-1} L \phi^p \tag{13}$$

The spatial derivatives are evaluated using second-order central differences. A cyclic variation of the pseudotime parameter is used to accelerate convergence.

The fluid equations, the drift-diffusion equations, and the Poisson equation are solved in a loosely coupled fashion inside a subiteration loop intended to drive $\Delta \bar{U}$ and $\Delta \phi$ toward zero. Typically, one to three overall subiterations are employed, with 10–1000 iterations of the Poisson solver within each overall subiteration.

Because of the disparate time scales involved in the fluid dynamic and electromagnetic phenomena occurring in these problems,

calculations can be costly in computer time. Efforts have been made to improve the speed of the computations. In the implementation of the factorized schemes, multilevel parallelism is exploited by using vectorization, multithreading with OpenMP commands [15], and multiblock decomposition implemented through MPI commands [16]. Further, the code is set up to run either in a time-accurate mode or with independent time steps for the different physics modules to accelerate convergence.

III. Glow Discharge

Three-dimensional computations of a parallel-plate discharge in the absence of bulk gas flow were carried out. The working gas was nitrogen, the bulk gas velocity was set to zero, the pressure was 670 Pa (about 5 torr), and the gas temperature held fixed at 293 K. The potential at the anode was taken to be zero, and the normal derivatives of all variables were set to zero on the side boundaries. The secondary emission coefficient was taken to be $\gamma = 0.1$.

The computational grid consisted of $51 \times 51 \times 51$ points, distributed over a $20 \times 40 \times 40$-mm rectangular domain, with grid clustering near the electrode surfaces. The applied voltage was taken to be $V = 2$ kV, and the external resistance was $R = 300$ kΩ. The resulting cathode voltage was $V_c = -548$ V, and the current was $I = 4.84$ mA.

The results are shown in Figs. 1 and 2. The basic structure of the discharge is illustrated in Fig. 1a, which shows an ion number density isosurface $n_i = 4 \times 10^{15}$ m^{-3}. The cathode lies in the $x = 0$ m plane, to the left and back in the figure, and the anode lies in the $x = 0.02$ m plane. The corresponding current lines (trajectories of the current density vector field) and the current density isosurface $j = 110$ A/m^2 are shown in Fig. 1b. Details of the center plane $z = 0.02$ m are shown in Figs. 2a–2c, which show, respectively, contours of the ion number density, electron number density, and electric potential. Figure 2d shows the corresponding current lines in the same plane. In each of these plots, the cathode corresponds to the left boundary and the anode to the right.

Overall, the solution shows typical features of the "normal glow" regime. The discharge is axisymmetric; this is a property of the solution, not an imposed condition. The peak ion concentration occurs in a disk-shaped region near the cathode surface. This region occupies only a portion of the cathode area. There is significant charge separation there, with a large concomitant potential drop. Between the cathode and anode layers lies a column of quasi-neutral plasma in which ion and electron concentrations are almost equal. Near the anode surface is a small region of finite space charge. The current lines originate at the anode, follow the plasma column across the discharge gap, then diverge as they pass through the cathode layer.

One-dimensional theory for the normal glow discharge [17] gives a cathode layer thickness of $d_n = 1.5$ mm and a corresponding potential drop of $V_n = 205$ V, which compare well with the computational results. This theory also predicts a normal current density of $j_n = 14$ A/m^2, which compares well with the average over the cathode spot of the computed current density ($I/A_{\text{spot}} = 19$ A/m^2), and is of the same order as the peak current density computed at the cathode ($j_n = 66$ A/m^2). Further, the computational values match well with the following experimental results for nitrogen at 670 Pa quoted in Raizer [17]: $d_n = 0.6$–0.8 mm, $V_n = 170$–233 V, and $j_n = 96$–101 A/m^2.

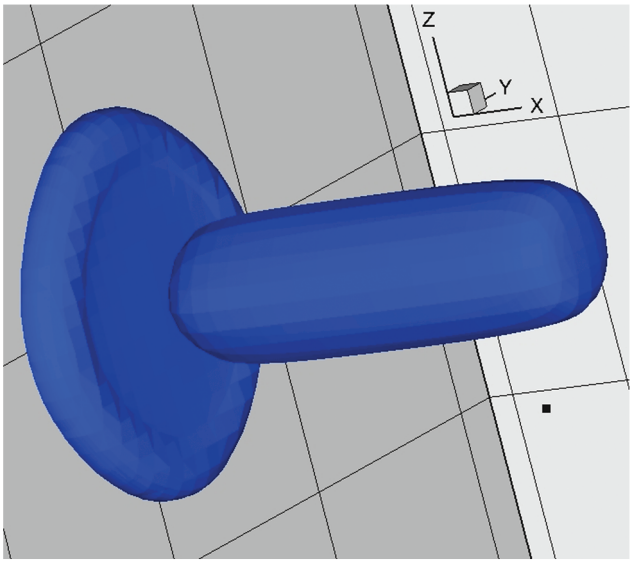

a) Ion number density isosurface $n_i = 4{:}0 \times 10^{15}$ m^{-3}

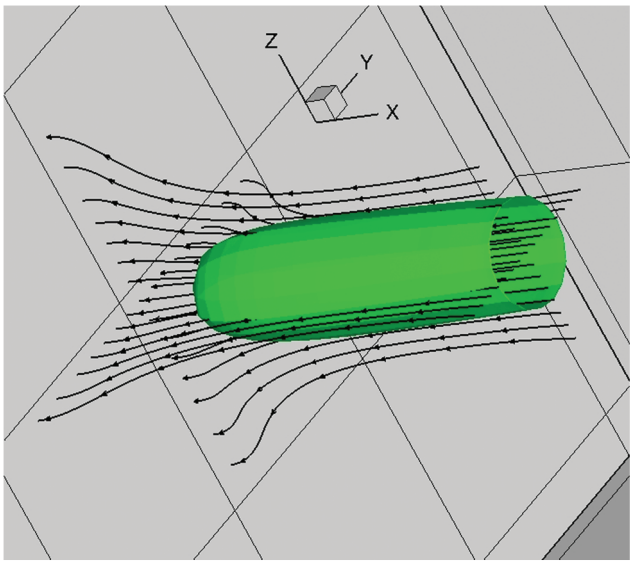

b) Current lines and current density isosurface $j = 110$ A/m^2

Fig. 1 Glow discharge at 670 Pa: three-dimensional views.

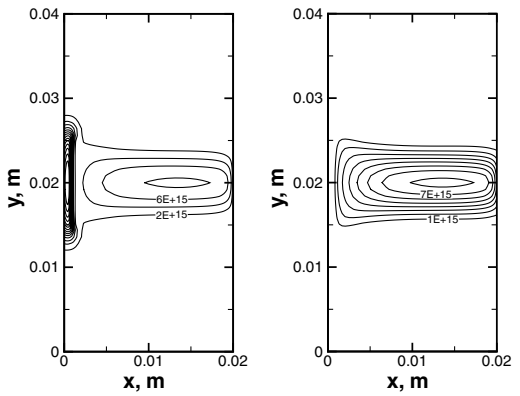

a) Ion number density **b) Electron number density**

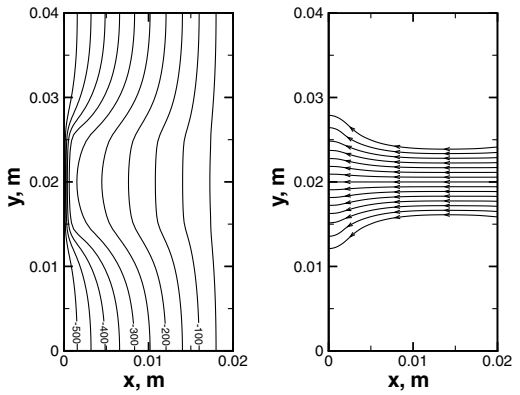

c) Electric potential **d) Current lines**

Fig. 2 Glow discharge at 670 Pa: center-plane contours.

IV. Boundary-Layer Control

A computational study was made of a configuration similar to that examined experimentally by Kimmel et al. [18]. The dimensions of the test article considered here are close to, but not exactly the same as, those considered in that study. The working fluid was taken to be nitrogen rather than air as in the experiments. The test article was a 66×38.1 − mm, sharp-edged flat plate. The freestream conditions were $p_\infty = 64$ Pa, $T_\infty = 43$ K, and $u_\infty = 688$ m/s. Adiabatic wall conditions were assumed.

A computational grid of $101 \times 81 \times 81$ points, distributed over a rectangular domain of dimensions $66 \times 25 \times 38.1$ mm, was considered. The cathode and anode were taken to be located on the plate surface ($y = 0$ mm), with a finite extent in the spanwise direction ($9.5 \leq z \leq 28.6$ mm). The cathode was located at a station upstream ($13.2 \leq x \leq 26.4$ mm), and the anode farther downstream (39.6 mm $\leq x \leq$ 52.8 mm). Grid clustering was employed near the electrode boundaries and near the plate surface. The cathode was held at $\phi = -1$ kV (no external load), and the secondary emission coefficient was taken to be $\gamma = 0.1$.

Figures 3a and 3b show three-dimensional perspective views of the computed solutions. For the case with the discharge on, contours of electric potential with selected current lines are shown in Fig. 3a, and corresponding isobars are shown in Fig. 3b. The bulk gas flow is in the positive x direction. When the discharge is on, a net current of about 0.4 A flows from the downstream anode to the upstream cathode.

For the baseline case, temperature and pressure are uniform in the spanwise direction. Significant changes in the solution are observed with the discharge on. Most of the potential variation occurs near the surface of the cathode and around its edges (Fig. 3a), and significant dissipative heating occurs in this region. In particular, a wall-temperature maximum appears near the downstream edge of the cathode, leading to boundary-layer thickening, and an associated compression wave system that emanates from the vicinity of the cathode. Wall pressure increases due to the presence of these waves.

Figures 4a and 4b show selected profiles through the solution, comparing the baseline case to the case with the discharge on. Figure 4a shows the centerline wall pressure profile ($y = 0$ mm, $z = 19$ mm). For the baseline case with the discharge off (dash-dot-dot line), the pressure distribution shows the expected decrease with a streamwise position. With the discharge on (solid line), a strong perturbation of the wall pressure occurs, starting at the cathode and peaking near its downstream edge. A similar effect appears in the centerline profile of the skin friction coefficient (Fig. 4b), with a drop in skin friction over the cathode and an overshooting recovery downstream.

Given the changes in pressure and skin friction, it is interesting to assess the overall effect of the discharge on the forces on the plate. Despite the initial decrease in skin friction over the cathode, the overshooting recovery leads to a 2% increase in drag on the plate. The overall downward force on the plate due to wall pressure increases by about 6% with the discharge on due to the increased flow compression with boundary-layer thickening.

Examining the source terms that appear in the fluid conservation laws, we find that the changes that the discharge introduces in the flow structure are primarily due to dissipative heating effects rather than the electric force on the bulk gas. The maximal values of the

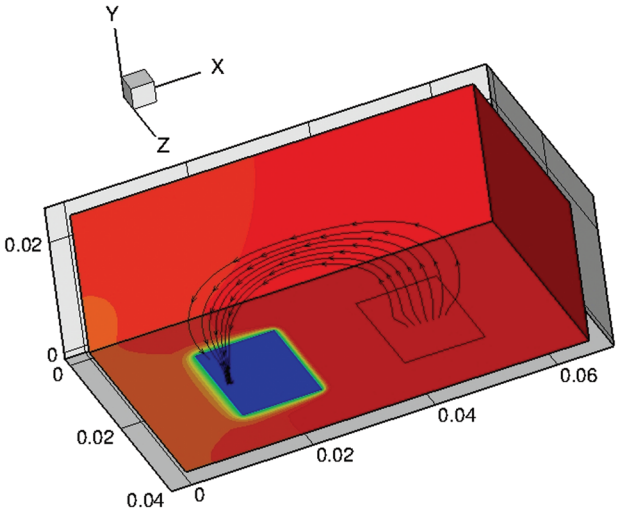

a) Potential distribution and current lines

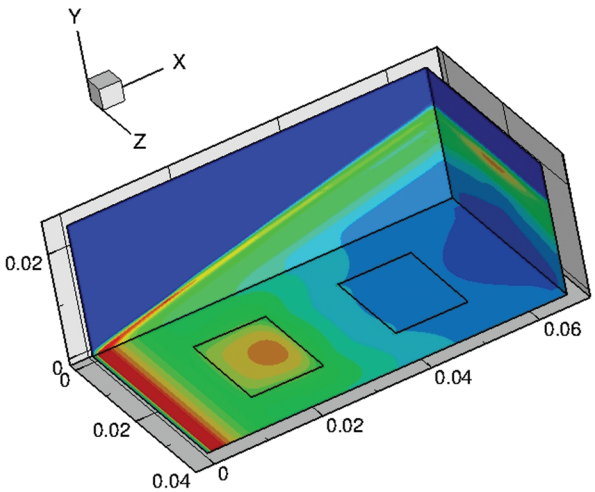

b) Pressure distribution

Fig. 3 Flat plate boundary-layer control: three-dimensional views.

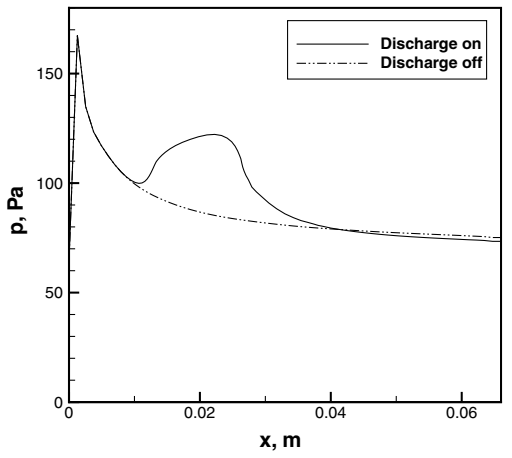

a) Wall pressure

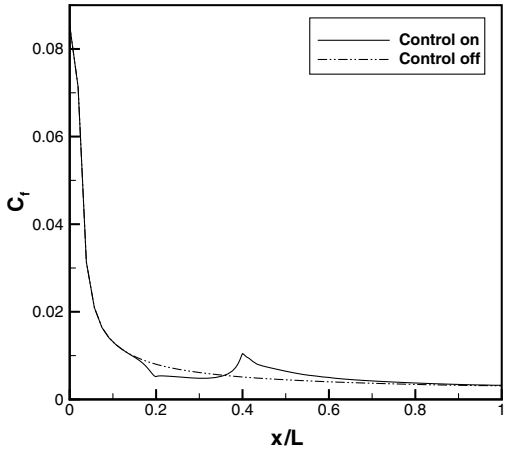

b) Skin friction

Fig. 4 Flat plate boundary-layer control: centerline profiles.

nondimensional source terms occur near the downstream edge of the cathode, where the electric field is high. The nondimensional electromagnetic power term $P = \eta \mathbf{E} \cdot \mathbf{j} L/(\rho_\infty u_\infty^3)$ has a maximum value of $P \approx 6$. In comparison, the maximum nondimensional rate of mechanical work done by the electric body force $P_m = \rho_c \mathbf{E} \cdot \mathbf{u} L/(\rho_\infty u_\infty^3)$ is 3 orders of magnitude smaller: $P_m \approx -0.006$. The maximum nondimensional value of the wall-normal component of the body force $f_y = \rho_c E_y L/(\rho_\infty u_\infty^2)$ is quite small ($f_y \approx -0.04$), and the other force components are completely negligible. Indeed, turning off the force term in the calculations had no discernible effect on the solution.

The results obtained here are qualitatively consistent with experimental observation of discharges [6,18] and simple heating [6,19] and with computations using simplified physical models based on gas dynamic heating [20–22] or quasi-neutral electromagnetics [22,23]. A preliminary comparison to experimental data [6] is made in Figs. 5a and 5b, which show centerline profiles of the total temperature with the discharge on, divided by the corresponding value of the total temperature when the discharge is off. It is important to note that the experimental data and computations do not correspond to exactly the same conditions: the electrode geometries are different (noted in the figures), and the working gas is different (air for the experiments, nitrogen for the computations). Nevertheless, qualitative agreement in trends is observed. The streamwise profile of $T_{0,\mathrm{on}}/T_{0,\mathrm{off}}$ is initially flat, then shows a rise at the cathode, followed by a slow decay downstream. The predicted rise in total temperature is within 20% of the experimental value.

Experiments by Menart et al. [6] show a linear relationship between the power input to the discharge and the effective angle of attack. Experimental data indicate that replacing a mechanical flap of 100-cm width, deflected 4 deg at Mach 5, requires a power input of 8 kW to the discharge. This is within the range of auxiliary power that might be available on a hypersonic glide test vehicle, so that further testing of this concept is warranted and feasible.

V. Shock Wave/Boundary-Layer Interaction

In Poggie [7], the computational cost of high-fidelity modeling was avoided by applying a simplified plasma actuator model to the study of the control of a separated compression ramp flow. The object of the study was to determine whether a modest power input consisting of dissipative heating or mechanical work localized near separation could lead to structural changes in the flow. With suitable power levels and locations identified, future work will examine the flow using the detailed discharge model.

The baseline flow was taken to be the Mach 14 compression ramp flow originally studied by Holden and Moselle [24]. The ramp configuration consisted of an initial flat plate of length $L = 0.439$ m and width $W = 0.610$ m mounted parallel to the freestream, followed by a second plate inclined to the freestream by an angle of $\theta = 24$ deg. The freestream conditions, upstream of the leading edge shock, were $M = 14.1$ and $Re_L = 1.04 \times 10^5$.

For comparison with the experimental data, three-dimensional calculations were carried out on $202 \times 60 \times 60$ and $404 \times 120 \times 120$ grids. The results are summarized in Fig. 6a, which compares the predicted heat transfer coefficient (Stanton number $C_h = q_w/[\rho_\infty U_\infty (H_\infty - H_w)]$) on the model centerline to the experimental data of Holden and Moselle [24]. The separation location is seen to be accurately predicted on the finer grid, but the peak heat transfer rate is somewhat overpredicted and occurs slightly upstream of that observed in the experimental data. Similar results

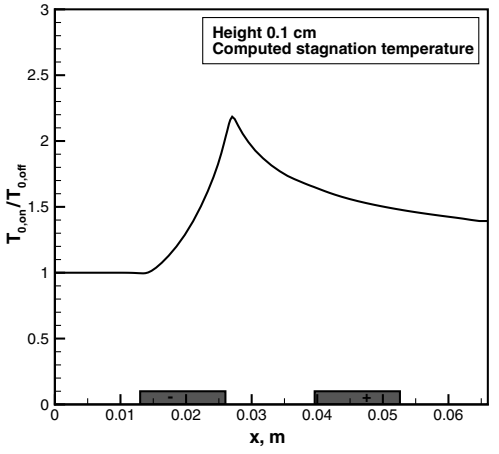

a) Computation

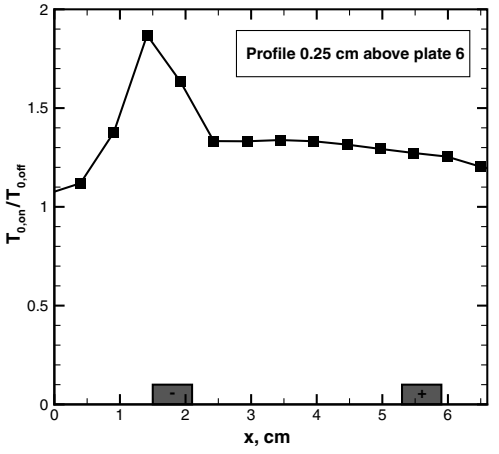

b) Measurement

Fig. 5 Flat plate boundary-layer control: profile of total temperature ratio.

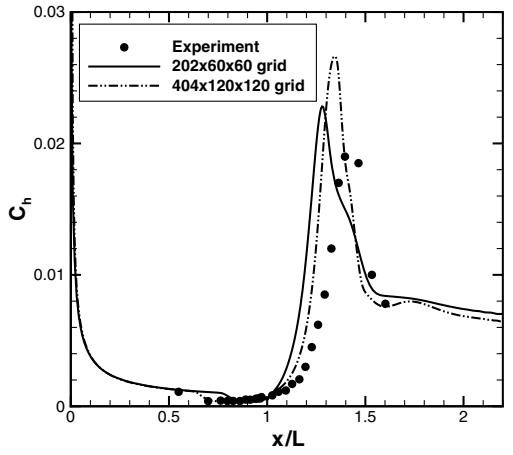

a) Baseline flow validation

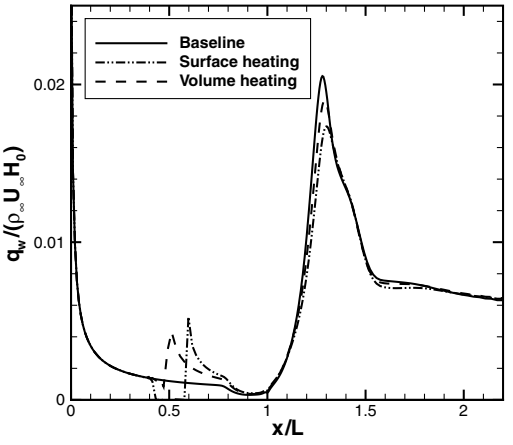

b) Effects of control

Fig. 6 Results of three-dimensional computations of 24-deg ramp flow: heat transfer coefficient on wall centerline.

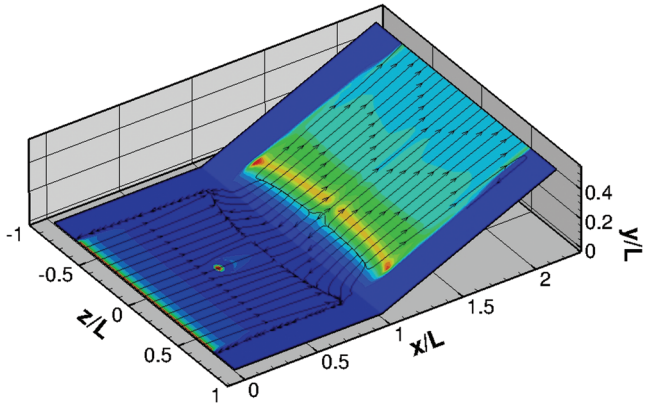

a) Surface heating

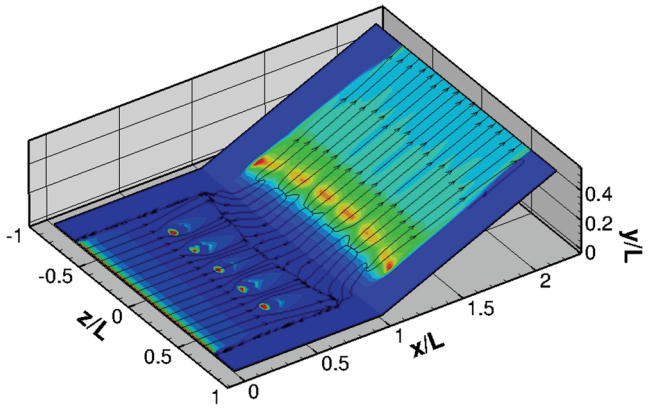

b) Surface heating x 5

Fig. 7 Results of three-dimensional computations of 24-deg ramp flow: skin friction lines and heat transfer rate contours at the wall.

have been observed in previous computational studies of this flow [25–30].

Phenomenological models of the dissipative heating S and body force $\mathbf{f}$ were considered [See Eqs. (2) and (3)], and their effects on the flow were evaluated. The volumetric heating model had the form

$$S = \frac{Q}{\pi^{3/2}a^3}\exp\left(-\frac{r^2}{a^2}\right) \tag{14}$$

and was added to the total energy equation (3). Here, the variable r represents the distance from the center of the heating, and Q is the total energy deposited by the source term. The applied body force had the analogous form

$$\mathbf{f} = \frac{2Q}{U_\infty \pi^{3/2}a^3}\exp\left(-\frac{r^2}{a^2}\right)\mathbf{e}_x \tag{15}$$

and was added to the momentum equation (2), with $\mathbf{f}\cdot\mathbf{u}$ added to the total energy equation (3). Note that this source term integrated over all space has the value $2Q/U_\infty$, so that the net mechanical power delivered to the fluid is about the same as the heating specified in Eq. (14). The surface-heating model had the form

$$q_w = \frac{Q}{\pi a^2}\exp\left(-\frac{r^2}{a^2}\right) \tag{16}$$

and was applied as a boundary condition. The definitions are changed here to reflect the nature of the surface source: the variable r represents the distance along the wall from the center of the heating, and the surface integral of q_w over the boundary gives the total energy deposited Q.

A series of exploratory studies of the effect of volumetric heating, body forces, and surface heating were carried out on a $202 \times 60 \times 60$ grid. The intensity of energy deposition was determined by the values $Q = 100$ W and $a = 0.005$ m, and the "actuators" were located on the centerline, halfway down the initial flat plate ($L/2 = 0.220$ m). The volumetric sources were centered 0.008 m from the wall.

The effects of each control case on the peak heating at reattachment are summarized in Table 1. It is seen that all the control cases, except the downstream and downward directed forces, significantly reduce the peak heat transfer rate.

The selected results for the effect of the heating-based control cases are shown in Fig. 6b. (Because of the varying wall and total temperatures, a modified heat transfer coefficient $C_h = q_w/[\rho_\infty U_\infty H_\infty]$ is shown.) The peak heat transfer rate downstream of reattachment is seen to be reduced for both cases shown, with only moderate changes to the rest of the profile. Some heat transfer penalty is incurred near the actuator location.

The control effects tended to be confined to a strip downstream with a characteristic width of the same order as that of the control actuator. Figures 7a and 7b show skin friction lines (trajectories of the wall shear stress vector field) and heat transfer coefficient for surface-heating cases with one and with five actuators. Control is seen to introduce a significant degree of spanwise nonuniformity. For the spacing considered here, multiple actuators did not seem to interfere with each other.

The heat transfer integrated over the surface $q_{\text{net}} = \iint \mathbf{q}_w \cdot \mathbf{n}\, \mathrm{d}S$ was computed to determine the net effect of each control case. Although significant local decreases in heat transfer have occurred (Table 1 and Figs. 7a and 7b), the net heat load remained nearly the same. The maximum change in total heat transfer was slightly over 1%, which occurred for the heating cases with five actuators. Close inspection of Figs. 7a and 7b indicates that the heat transfer is strongly reduced directly downstream of each actuator near the reattachment hot spot, but outboard of that region the heat transfer is moderately increased over a large area. Thus, this form of control may be useful for mitigating local hot spots but appears to have a negligible effect on the net heat transfer.

VI. Conclusions

Numerical studies of glow discharges were carried out to evaluate their utility for flow control applications. As part of this project, a three-dimensional computer code has been written to solve, in an implicit, loosely coupled fashion, the fluid conservation laws, the

Table 1 Conditions at peak reattachment heating ($z/L = 0$): effect of control

Case	x/L	C_f	$C_h = \frac{q_w}{\rho_\infty U_\infty H_\infty}$	C_p
Baseline	1.28	2.25×10^{-2}	2.05×10^{-2}	0.741
Surface heating	1.30	1.58×10^{-2}	1.73×10^{-2}	0.668
Surface heating × 5	1.32	1.77×10^{-2}	1.80×10^{-2}	0.731
Volumetric heating	1.29	1.86×10^{-2}	1.90×10^{-2}	0.707
Volumetric heating × 5	1.30	1.97×10^{-2}	1.91×10^{-2}	0.741
Downstream force	1.27	2.59×10^{-2}	2.19×10^{-2}	0.731
Downstream force and volume heating, 50 W each	1.28	2.15×10^{-2}	2.03×10^{-2}	0.722
Upstream force	1.30	1.83×10^{-2}	1.86×10^{-2}	0.723
Upward force	1.32	1.70×10^{-2}	1.69×10^{-2}	0.709
Downward force	1.27	2.80×10^{-2}	2.27×10^{-2}	0.766

charged particle continuity equations under the drift-diffusion model, and the Poisson equation for the electric potential. Several numerical techniques, including proper evaluation of the source terms and implicit procedures, have proven to be critical to successful high-fidelity simulations.

Fully three-dimensional calculations have been carried out using a detailed physical model for dc discharges in nitrogen. First, glow discharge calculations were carried out in the absence of flow, exploring the effects of background pressure, applied magnetic fields, and finite electrodes. These calculations serve as a rudimentary validation of the numerical code.

The glow discharge model was then applied to a relatively realistic flow control actuator in a Mach 5 boundary-layer flow. This device is a simple plasma flap in which an electrical input produces a control force. The mechanism for the downward force observed experimentally was identified through the numerical computations: dissipative heating near the cathode leads to boundary-layer thickening, compression waves, and a net wall pressure increase. The measured rise in total temperature was predicted within about 20%, an excellent result considering the many simplifications included in the theoretical model. Although the simplifications used in these calculations preclude an exact match with experiment, the fidelity of the model is now sufficient to understand the mechanism for the operation of the device.

Finally, the control of a Mach 14 compression ramp flow was explored using a simplified plasma actuator model. Acceptable agreement was obtained between computation and experiment for the baseline heat transfer distribution. Control was applied just upstream of separation. The peak heat transfer rate was reduced substantially by surface or volumetric heating, and by an upstream- or upward-directed body force. Suitable actuator locations and power levels have been identified, and future work will address this flow with the detailed discharge model.

Emphasis in this research program has been placed on three-dimensional modeling at different levels of fidelity. Despite the simplifications introduced in the theory, the disparity in time scales between the plasma behavior and the bulk gas flow behavior make modeling the plasma actuator an inherently computationally expensive problem. Improved algorithms for solving the particle continuity/Poisson system of equations could enable routine engineering calculations of actuator performance.

Acknowledgments

This work has been sponsored in part by grants from the Air Force Office of Scientific Research (monitored by J. Schmisseur and F. Fahroo) and by grants of High Performance Computing time from several of the Department of Defense Major Shared Resource Centers. The author would like to acknowledge helpful discussions over the years with his colleagues at the Air Force Research Laboratory Computational Sciences Branch and with I. Adamovich, W. Hilbun, R. Kimmel, S. Macheret, J. Shang, M. Shneider, N. Sternberg, and S. Surzhikov.

References

[1] Poggie, J., and Sternberg, N., "Numerical Simulation of Glow Discharges for High-Speed Flow Control," AIAA Paper 2004-0177, Jan. 2004.

[2] Poggie, J., "Numerical Exploration of Flow Control with Glow Discharges," AIAA Paper 2004-2658, June 2004.

[3] Poggie, J., "Implicit, Approximately-Factored, Upwind Scheme for Glow Discharge Modeling," *Computational Fluid and Solid Mechanics 2005*, edited by K. J. Bathe, Elsevier, Amsterdam, 2005, pp. 998–1000.

[4] Poggie, J., "Computational Studies of High-Speed Flow Control with Weakly-Ionized Plasma," AIAA Paper 2005-0784, Jan. 2005.

[5] Poggie, J., "DC Glow Discharges: A Computational Study for Flow Control Applications," AIAA Paper 2005-5303, June 2005.

[6] Menart, J., Henderson, S., Atzbach, C., Shang, J., Kimmel, R., and Hayes, J., "Study of Surface and Volumetric Heating Effects in a Mach 5 Flow," AIAA Paper 2003-2262, June 2003.

[7] Poggie, J., "Plasma-Based Control of Shock-Wave /Boundary-Layer Interaction," AIAA Paper 2006-1007, Jan. 2006.

[8] Surzhikov, S. T., "Numerical Simulation of Two-Dimensional Structure of Glow Discharge in View of the Heating of Neutral Gas," *High Temperature*, Vol. 43, No. 6, 2005, pp. 825–842. doi:10.1007/s10740-005-0130-4

[9] Surzhikov, S. T., and Shang, J. S., "Two-Component Plasma Model for Two-Dimensional Glow Discharge in Magnetic Field," *Journal of Computational Physics*, Vol. 199, No. 2, 2004, pp. 437–464. doi:10.1016/j.jcp.2004.02.019

[10] Beam, R. M., and Warming, R. F., "An Implicit Factored Scheme for the Compressible Navier-Stokes Equations," *AIAA Journal*, Vol. 16, No. 4, 1978, pp. 393–402.

[11] Pulliam, T. H., and Steger, J. L., "Implicit Finite-Difference Simulations of Three-Dimensional Compressible Flow," *AIAA Journal*, Vol. 18, No. 2, 1980, pp. 159–167.

[12] Jameson, A., Schmidt, W., and Turkel, E., "Numerical Solutions of the Euler Equations by a Finite Volume Method Using Runge–Kutta Time Stepping Schemes," AIAA Paper 81-1259, 1981.

[13] Holst, T. L., "On Approximate Factorization Schemes for Solving the Full Potential Equation," NASA TM 110435, 1997.

[14] Holst, T. L., "Transonic Flow Computations Using Nonlinear Potential Methods," *Progress in Aerospace Sciences*, Vol. 36, No. 1, 2000, pp. 1–61. doi:10.1016/S0376-0421(99)00010-X

[15] Chandra, R., Dagum, L., Kohr, D., Maydan, D., McDonald, J., and Menon, R., *Parallel Programming in OpenMP*, Academic Press, San Diego, CA, 2001.

[16] Gropp, W., Lusk, E., and Skjellum, A., *Using MPI: Portable Parallel Programming with the Message-Passing Interface*, 2nd ed., MIT Press, Cambridge, MA, 1999.

[17] Raizer, Y. P., *Gas Discharge Physics*, Springer–Verlag, Berlin, 1991.

[18] Kimmel, R. L., Hayes, J. R., Menart, J. A., and Shang, J., "Effect of Surface Plasma Discharges on Boundary Layers at Mach 5," AIAA Paper 2004-0509, Jan. 2004.

[19] Debiève, J.-F., Dupont, P., Smith, D. R., and Smits, A. J., "Supersonic Turbulent Boundary Layer Subject to Step Changes in Wall Temperature," *AIAA Journal*, Vol. 35, No. 1, 1997, pp. 51–57.

[20] Levin, V. A., and Larin, O. B., "Skin-Friction Reduction by Energy Addition into a Turbulent Boundary Layer," AIAA Paper 2003-0036, Jan. 2003.

[21] Leonov, S., Yarantsev, D., Kuryachii, A., and Yuriev, A., "Study of Friction and Separation Control by Surface Plasma," AIAA Paper 2004-0512, Jan. 2004.

[22] Shang, J. S., Gaitonde, D. V., and Updike, G. A., "Modeling Magneto-Aerodynamic Actuator for Hypersonic Flow Control," AIAA Paper 2004-2657, June 2004.

[23] Shang, J. S., and Surzhikov, S. T., "Magneto-Fluid-Dynamics Interaction for Hypersonic Flow Control," AIAA Paper 2004-0508, Jan. 2004.

[24] Holden, M. S., and Moselle, J. R., "Theoretical and Experimental Studies of the Shock Wave—Boundary Layer Interaction on Compression Surfaces in Hypersonic Flow," Aerospace Research Laboratories, TR ARL 70-0002, Jan. 1970.

[25] Hung, C. M., and MacCormack, R. W., "Numerical Solutions of Supersonic and Hypersonic Laminar Compression Ramp Flows," *AIAA Journal*, Vol. 14, No. 4, 1976, pp. 475–481.

[26] Power, G. D., and Barber, T. J., "Analysis of Complex Hypersonic Flows with Strong Viscous/Inviscid Interaction," *AIAA Journal*, Vol. 26, No. 7, 1988, pp. 832–840.

[27] Rizzetta, D., and Mach, K., "Comparative Numerical Study of Hypersonic Compression Ramp Flows," AIAA Paper 89-1877, June 1989.

[28] Rudy, D. H., Thomas, J. L., Kumar, A., Gnoffo, P. A., and Chakravarthy, S. R., "Computation of Laminar Hypersonic Compression-Corner Flows," *AIAA Journal*, Vol. 29, No. 7, 1991, pp. 1108–1113.

[29] Gaitonde, D., and Shang, J. S., "The Performance of Flux-Split Algorithms in High-Speed Viscous Flows," AIAA Paper 92-0186, Jan. 1992.

[30] Updike, G. A., Shang, J. S., and Gaitonde, D. V., "Hypersonic Separated Flow Control Using Magneto-Aerodynamic Interaction," AIAA Paper 2005-0164, Jan. 2005.

S. Macheret
Guest Editor